

RESEARCH ARTICLE

10.1002/2015JB012677

Key Points:

- Magnetotellurics is a useful tool for imaging subglacial structures
- A distinct boundary between the Vestfold Hills and the Rauer Group lies beneath the Sørsdal Glacier
- Time-frequency analysis characterizes magnetic source fields

Supporting Information:

- Movie S1
- Data Set S1
- Data Set S2
- Supporting Information S1

Correspondence to:

J. R. Peacock,
jpeacock@usgs.gov

Citation:

Peacock, J. R., and K. Selway (2016), Magnetotelluric investigation of the Vestfold Hills and Rauer Group, East Antarctica, *J. Geophys. Res. Solid Earth*, 121, 2258–2273, doi:10.1002/2015JB012677.

Received 20 NOV 2015

Accepted 31 MAR 2016

Accepted article online 5 APR 2016

Published online 26 APR 2016

Magnetotelluric investigation of the Vestfold Hills and Rauer Group, East Antarctica

J. R. Peacock^{1,2} and K. Selway^{2,3}
¹U.S. Geological Survey, Menlo Park, California, USA, ²Department of Earth Sciences, Formerly at the University of Adelaide, Adelaide, South Australia, Australia, ³Centre for Earth Evolution and Dynamics, University of Oslo, Oslo, Norway

Abstract The Vestfold Hills and Rauer Group in East Antarctica have contrasting Archean to Neoproterozoic geological histories and are believed to be juxtaposed along a suture zone that now lies beneath the Sørsdal Glacier. Exact location and age of this suture zone are unknown, as is its relationship to regional deformation associated with the amalgamation of East Gondwana. To image the suture zone, magnetotelluric (MT) data were collected in Prydz Bay, East Antarctica, mainly along a profile crossing the Sørsdal Glacier and regions inland of the Vestfold Hills and Rauer Group islands. Time-frequency analysis of the MT time series yielded three important observations: (1) Wind speeds in excess of ~8 m/s reduce coherence between electric and magnetic fields due to charged wind-blown particles of ice and snow. (2) Estimation of the MT transfer function is best between 1000 and 1400 UT when ionospheric Hall currents enhance the magnetic source field. (3) Nonplanar source field effects were minimal but detectable and removed from estimation of the MT transfer function. Inversions of MT data in 2-D and 3-D produce similar resistivity models, where structures in the preferred 3-D resistivity model correlate strongly with regional magnetic data. The electrically conductive Rauer Group is separated from the less conductive Vestfold Hills by a resistive zone under the Sørsdal Glacier, which is interpreted to be caused by oxidation during suturing. Though a suture zone has been imaged, no time constraints on suturing can be made from the MT data.

1. Introduction

Thick ice covers nearly all of Antarctica; thus, geophysical methods are required to image sub-ice geological structures. Magnetotellurics (MT) is a passive electromagnetic method that is an important geophysical technique for investigating sub-ice structure in Antarctica as it combines good resolution, minimal environmental impact, and favorable logistics [e.g., *Beblo and Liebig*, 1990; *Wannamaker et al.*, 2004; *Murthy et al.*, 2013].

However, collection of MT data in Antarctica faces three main challenges. The first challenge is high contact resistance between electrodes and ice, where capacitance and contact impedance along the electric dipole line interact causing distortion through complex voltage dividers and capacitive coupling, which generate large measurement errors. The first MT measurements in Antarctica were described by *Hessler and Jacobs* [1966], who deployed a single station at Vostock and demonstrated that long-period electric field measurements are possible despite the very high (>10 MΩ) contact resistance of ice. Nevertheless, to reduce effects of the high impedance on electric field data, *Wannamaker et al.* [1996] developed preamplifiers to allow wideband data to be collected on ice. The authors used the preamplifiers to successfully collect 12 stations over the Byrd Subglacial Basin and 10 additional stations in a follow-up survey along a profile at the South Pole [*Wannamaker et al.*, 2004]. The second challenge is proximity to the geomagnetic south pole, which can violate the inherent assumption of the MT method that the magnetic source field is a vertically impinging, horizontally polarized plane wave [e.g., *Pirjola*, 1992]. Analysis of magnetic source field effects from previous surveys by *Beblo and Liebig* [1990] of 4 stations in North Victoria Land and 10 stations at the South Pole by *Wannamaker et al.* [2004] did not find any significant effects on the MT response for periods less than 4000 s. The third challenge, observed by *Wannamaker et al.* [2004], is that wind-blown, statically charged ice particles produce significant noise in the measured electric fields when wind speeds are high. These three challenges need to be taken into consideration when collecting MT data in Antarctica.

The goal of this project was to further investigate the applicability of MT for imaging sub-ice geological structures in Antarctica, with two research goals. The first goal was to assess source field effects and the effects of

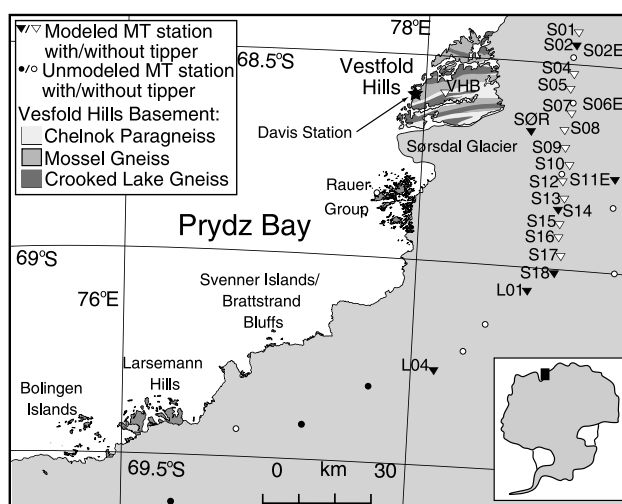


Figure 1. Map of survey area in Prydz Bay, East Antarctica, adapted from *Kelsey et al.* [2008]. Basement geology of the Vestfold Hills is simplified from *Hoek and Seitz* [1995].

wind-blown particles on MT data and to test whether these challenges could be overcome to collect accurate and precise MT data. The second goal was to use the MT data to locate a possible suture zone in the Prydz Bay region of East Antarctica. This region was chosen for its inherent geological importance and also because its proximity to Australia's Davis Station allowed us to address the methodological questions in a location with good helicopter and logistical support before attempting more challenging, deep field surveys.

2. Prydz Bay Geology

The Neoproterozoic assemblage of East Gondwana included parts of the present-day Antarctica, Australia, India, and southern Africa [Collins and Pisarevsky, 2005]. This supercontinent assembled through a complex series of orogenic events spanning the period circa 750–530 Ma [Meert, 2003]. However, the geographic extents of precursor continents to East Antarctica and the locations of suture zones between them remain poorly constrained. A striking example of this is in the Prydz Bay coast and Prince Charles Mountains, where many outcropping rocks correlate with known geology in India [e.g., Black et al., 1987; Harley and Fitzsimons, 1995; Kinny et al., 1997; Rickers et al., 2001]; however, dramatically different interpretations of the Indian paleocontinent's inland extent into the present-day East Antarctica have been proposed [Boger et al., 2001; Harley, 2003].

The main geological regions of Prydz Bay are, from northeast to southwest, the Vestfold Hills, the Rauer Group, the Svenner Islands/Brattstrand Bluffs, the Larsemann Hills, and the Bolingen Islands (Figure 1). Lithologies in the Svenner Islands/Brattstrand Bluffs, the Larsemann Hills, and the Bolingen Islands in southwest Prydz Bay are dominated by Grenvillean (circa 1200–900 Ma) and Ediacaran-Cambrian (circa 600–510 Ma) deposition, magmatism, and pervasive metamorphism, with few or no older protoliths recorded [Harley, 2003]. The Ediacaran-Cambrian tectonism is temporally coincident with the Pan-African and Pinjarra Orogenies that assembled East Gondwana [Collins and Pisarevsky, 2005].

Basement rocks in the Vestfold Hills and adjacent Rauer Group contrast with each other and with those further south in Prydz Bay. The Rauer Group records Archean protoliths (3270 Ma, 2840 Ma, and 2800 Ma), tectonism (3470–3270 Ma and 2944 Ma), and Mesoproterozoic intrusion of mafic dikes and sediment deposition [Harley et al., 1998]. Events recorded within younger lithologies in the Rauer Group correlate more closely with those in southwest Prydz Bay, including ultrahigh-temperature metamorphism at circa 1170–910 Ma, basin development at circa 600–575 Ma [Kelsey et al., 2008], and granulite-facies metamorphism at circa 570–510 Ma [Kelsey et al., 2003; Wilson et al., 2007]. The Vestfold Hills contain basement rocks with circa 2575–2515 Ma protoliths (the Chelnok and Taynaya Paragneisses), which were deformed at circa 2520–2445 Ma and roughly contemporaneous with the emplacement of 2520–2470 Ma protoliths to the Mossel Gneiss and Crooked Lake Group [Clark et al., 2012; Flowerdew et al., 2013]. These rocks were intruded by multiple generations of mafic dikes

between 2240 Ma and 1241 Ma [Lanyon *et al.*, 1993]. Some evidence for Mesoproterozoic to Neoproterozoic (circa 900–650 Ma) metamorphism exists in the southern Vestfold Hills [Clark *et al.*, 2012], but the bulk of the Vestfold Hills basement shows no evidence for Mesoproterozoic to Neoproterozoic deformation. In strong contrast to the rest of Prydz Bay, the Vestfold Hills were not affected by Pan-African aged deformation [Harley, 2003].

The disparate Archean and Proterozoic evolutions of the Vestfold Hills and Rauer Block suggest that they are allochthonous terranes that were juxtaposed relatively recently. The absence of Pan-African aged deformation in the outcropping Vestfold Hills is curious and suggests that suturing may have occurred late in Gondwana amalgamation [Boger *et al.*, 2001], while the presence of Mesoproterozoic to Neoproterozoic metamorphism raises the possibility that suturing may have occurred during the Grenvillian [Moore, 1991]. Outcrops of the Vestfold Hills and the Rauer Group are separated by the Sørsdal Glacier, which presumably overlies the suture between them.

While further geological and geochronological data are necessary to constrain the timing of suturing, geophysical data can be utilized to determine the location and nature of the suture, though little data currently exist. Magnetic data show a broad magnetic high that covers both the Rauer Group and most of the Vestfold Hills with a decrease in magnetic susceptibility along the Sørsdal Glacier [Golynsky *et al.*, 2002, 2006a; McLean *et al.*, 2009]. Seismic receiver functions show a crustal thickness of 36 km in the Vestfold Hills and similar crustal thicknesses of 30–35 km southwest along Prydz Bay [Reading, 2006].

3. MT Method

MT is a passive method that measures the Earth's electrical response to natural, time-varying magnetic fields [Kaufman and Keller, 1981; Chave and Jones, 2012]. Formally, the MT transfer function or impedance tensor \mathbf{Z} is defined by equation (1), where \mathbf{E} is the electric field \mathbf{E} and \mathbf{H} is the magnetic field as measured at the surface. \mathbf{Z} is a complex, frequency-dependent, rank two tensor that contains all the information about subsurface resistivity structure. From \mathbf{Z} , the apparent resistivity and impedance phase can be calculated. At a given period, the apparent resistivity is the resistivity equivalent to that of a homogeneous subsurface where the penetration depth can be estimated by the skin depth, which increases with period and subsurface resistivity. The impedance phase relates the phase difference between the inducing magnetic field and the induced electric field. Another useful representation of the MT response is the phase tensor Φ , defined as the matrix inverses of the imaginary part of the impedance tensor to the real part ($\Phi = \Re\{\mathbf{Z}\}^{-1} \Im\{\mathbf{Z}\}$) [Caldwell *et al.*, 2004]. The phase tensor is unaffected by galvanic distortions caused by near-surface inhomogeneities, which can be exploited to estimate and remove distortion from \mathbf{Z} [Bibby *et al.*, 2005].

$$\begin{pmatrix} E_x \\ E_y \end{pmatrix} = \begin{pmatrix} Z_{xx} & Z_{xy} \\ Z_{yx} & Z_{yy} \end{pmatrix} \begin{pmatrix} H_x \\ H_y \end{pmatrix} \quad (1)$$

In an electrically 1-D Earth, the diagonal components of \mathbf{Z} will be zero and the off-diagonal components will be equal but opposite in sign; thus, the phase tensors will be represented as circles. In a 2-D Earth, where the measured \mathbf{E} and \mathbf{H} fields are parallel and perpendicular to geoelectric strike, the diagonal components of \mathbf{Z} will remain zero while the off-diagonal components will decompose into the transverse electric (TE) mode, where the electric field is parallel to geoelectric strike, and the transverse magnetic (TM) mode, where the magnetic field is parallel to geoelectric strike. The phase tensors for a 2-D Earth will be ellipses elongated in the preferred direction of current flow. In a 3-D Earth, all components of \mathbf{Z} will be nonzero and the phase tensors will be ellipses elongated in a skewed direction of current flow [Booker, 2014].

Similar to MT, geomagnetic depth soundings linearly relate the measured vertical magnetic field (H_z) to measured horizontal magnetic fields (\mathbf{H}) through a frequency-dependent complex magnetic transfer function (\mathbf{W}) by: $H_z(\omega) = \mathbf{W}(\omega)\mathbf{H}(\omega)$ [Parkinson, 1983]. Induced electrical currents that flow in strong subsurface conductors, particularly along elongated structures where current flows in a preferred geoelectric strike direction, create vertical magnetic fields. Graphically, \mathbf{W} can be represented by induction arrow whose real part points toward good conductors (in the Parkinson convention) and imaginary part provides information about the dimensionality of the conductive anomaly. Arrow length represents the strength of vertical magnetic fields. Induction arrows are useful for locating lateral boundaries of subsurface conductors.

4. Experiment

MT data were collected by a team from University of Adelaide with support from the Australian Antarctic Division (AAD) in the austral summer of 2008/2009. Thirty four stations were collected along three transects totaling approximately 200 line kilometers, with station spacing varying between 2.5 and 20 km. Instrumentation consisted of six AuScope MT systems using Numeric Resources preamplifiers [Wannamaker *et al.*, 2004] to overcome the high contact impedance of ice. Magnetic data were variably collected using three-component fluxgate, and two-component (both horizontal) and three-component (two horizontal and one vertical) induction coil magnetometers. Stainless steel plates were used for electrodes (with the face placed horizontally in snow or ice) along 100 m dipoles setup in an L-shape. Data were collected for an average of 5 days at a sampling rate of 100 samples/s. All stations were aligned with geomagnetic north (81° west of geographic north). The field team was stationed at the AAD's Davis Station and transported between stations via helicopter.

5. Data Analysis

One key assumption of the MT method is that the magnetic source field is a horizontally polarized plane wave propagating vertically toward the Earth, which can be violated in Antarctica due to its proximity to the geomagnetic south pole. Understanding the magnetic source field is of utmost importance when conducting any type of magnetic survey in polar regions [e.g., Pirjola, 1992; Jones and Spratt, 2002; Wannamaker *et al.*, 2004]. Robust processing schemes can effectively remove outliers within the data, including those associated with noncoherent noise [Larsen *et al.*, 1996; Egbert, 1997, 2002; Chave and Thomson, 2004], such as short (<10 s), sporadic pulsations or geomagnetic storms. However, processing only those time windows when source field effects are absent increases accuracy of estimated transfer functions. Time-frequency analysis provides a quantitative and qualitative characterization of the data, highlighting times when nonstationary, nonplanar sources are present [Chant and Hastie, 1992; Chi and Russell, 2008], which can aid in understanding the source field covariant in time, frequency, and space (Appendix A).

5.1. MT Transfer Function Estimation

An important part of estimating the MT transfer function is eliminating times when the magnetic source field is nonplanar. In this experiment, time-frequency analysis of time series data is used to eliminate times when source field effects are detected. The good time windows are then processed using the BIRRP code of Chave and Thomson [2004] to estimate the MT transfer function.

Pirjola [1992] demonstrates that source field effects in polar regions typically occur at periods longer than 60 s; here, a conservative range of periods are analyzed (2–3000 s) by downsampling time series data to 1 sample/s and 0.1 samples/s. Time-frequency distributions of each measured field were calculated by splitting time series data of the two sampling rates into windows of 512 points that overlap by 256 points with an L value of 11 (see Appendix A). This insures that the window is of optimal size to estimate the period range of interest (2–1000 s) and optimizes the spectrogram resolution. From the time-frequency distributions, four covariant parameters can be estimated to detect good times to estimate the MT transfer function in which source effects are minimal. For the remainder of this paper, the term “covariant” refers to a parameter that changes both in time and frequency.

The first parameter calculated, and the most revealing, is the covariant apparent resistivity ρ_a (equation (2)),

$$\rho_a^{ij}(\omega, t) = \frac{1}{\mu_0 \omega} |Z_{ij}(\omega, t)|^2 \quad (2)$$

where ω is angular frequency, μ_0 is the magnetic susceptibility of free space, and i and j are components of the measured horizontal magnetic and electric fields, respectively. The key assumption here is that apparent resistivity of the subsurface is time invariant [Banks, 1998]. This assumption is valid in most geologic settings and would only be violated in extreme cases such as sudden intrusion of conductive material (e.g., saline fluids or partial melt), which is highly unlikely in the tectonically stable study area. If the apparent resistivity varied by more than two standard deviations from the entire spectrogram within a given time window, the data are deemed invalid and removed from estimation of the MT transfer function.

The second parameter calculated was coherence between the measured electric field and the predicted electric field from the measured magnetic field based on Faraday's law of induction. When the predicted and

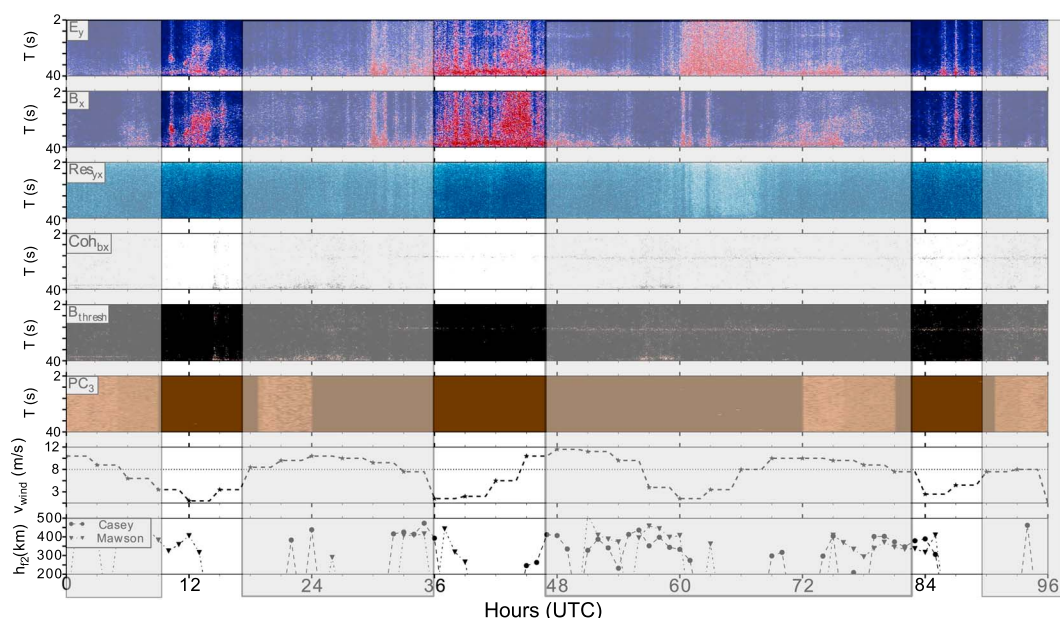


Figure 2. Example of good time windows to estimate the MT transfer function by estimating covariant parameters as described in section 5.1 for station S07. Warm colors and whites represent high values. From top to bottom plotted are the spectrograms for E_y and B_x , the apparent resistivity (equation (2)), coherence, threshold of B_z , the third principal component of the magnetic fields, ground wind speed, and height of the F_2 layer. Grayed out areas are excluded time windows for estimating the MT transfer function as seen in Figure 3.

measured fields had a coherence of less than 0.5, the time window was removed from estimation of the MT transfer function. Coherence estimation is also incorporated in the processing code of *Chave and Thomson* [2004], which was used to estimate the MT transfer function, and is used here as a complimentary parameter. It must be noted that in the presence of correlated noise, the coherence can give false positives and should only be used as a supplementary diagnostic.

The third covariant parameter calculated was formulated by *Jones and Spratt* [2002], in which a threshold on the magnitude of the vertical component of the magnetic field (in nT) is used as a source field gage (equation (3)), where σ is the standard deviation of the vertical magnetic field amplitude for the given time window and $B_{x,y,z}$ are the instantaneous amplitudes of the magnetic field components. If equation (3) is true, then it is assumed that the source field is nonplanar. For stations where B_z was not measured (Figure 1), observatory data from Davis Station were used as a proxy. This method works in areas where horizontal electrical currents are small, and thus, induction vectors are small, as in this study. In areas where induction vectors are large, the method outlined by *Wannamaker et al.* [2004] of removing outliers in the magnetic transfer function W is more robust.

$$1.5 \times \sigma \leq \frac{B_z(\omega, t)}{\sqrt{B_x(\omega, t)^2 + B_y(\omega, t)^2}} \quad (3)$$

The final parameter was estimated by using principal component analysis (PCA) of the measured magnetic fields. The key assumption is that only two principal components should exist for planar sources [*Egbert*, 2002]; in the absence of other noise sources, more than two principal components imply that nonplanar source field effects are present. Any time window when a third principal component is within a standard deviation of the first two principal components, it is assumed to have source field effects and is removed from MT transfer function estimation.

These four parameters were calculated for all components of each station, covering 51 days of observations, to find good times to estimate the MT transfer function (see Figures 2 and 3 as examples). The analysis focused on 22 stations with the highest-quality MT transfer functions, which were mostly broadband stations. Four observations were made after analyzing the data in this way. First, when surface wind speeds are above 8 m/s, electric field data become saturated by electrical signals generated by wind-blown snow particles in

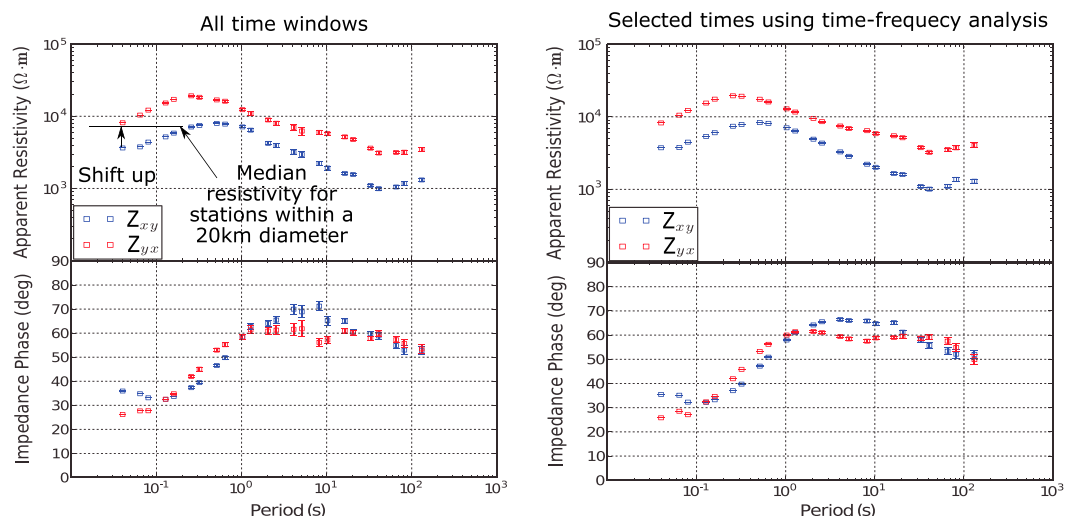


Figure 3. Example of MT transfer function estimation when all data are included and when time windows that may be affected by source field effects are removed as in Figure 2. The left plot also illustrates the method used to remove static shift.

the period range 2–100 s, similar to the findings of Wannamaker *et al.* [2004], resulting in reduced coherence and biased estimation of apparent resistivity. Second, estimation of covariant apparent resistivity revealed more time windows when source field effects were present. Third, PCA results reveal only two significant eigenvalues (>1 dB in signal-to-noise ratio) virtually all the time, suggesting that there are no extra magnetic sources, a similar result as found in Smirnov and Egbert [2012]. Fourth, estimated coherence values are above 0.8 for all periods daily between 1000 and 1400 UT and apparent resistivity values are stable. During this time there is a pronounced signal between 2 and 40 s (0.05–0.5 Hz) in the magnetic channels (Figure 4).

Some static shifts were observed in the data, all of which were from stations in heavily crevassed areas. Although distortion was removed from the data following Bibby *et al.* [2005], this does not necessarily remove static shift. As pointed out by Taylor *et al.* [1993], the resistivity of ice can vary depending on dust contamination. Here a spatial median filter was applied to remove static shifts. Diameter of the median filter was chosen to be 20 km, where the assumption is made that contamination of dust will be equivalent over this area. Any station within the median filter area was shifted to the median resistivity value with in the period range of 0.04–0.1 s of that area (Figure 3).

5.2. Dimensional Analysis

Dimensionality of the MT response can give an indication of complexity of the subsurface resistivity structure and prescribe the number of model dimensions needed [Martí, 2014]. Here dimensionality of the data was estimated from the phase tensor [Caldwell *et al.*, 2004] by determining the ellipticity (ϵ) [Bibby *et al.*, 2005] and the normalized skew angle Ψ of Booker [2014]. Generally, if $\epsilon > 0.1$, subsurface electrical structure is at least 2-D and is possibly anisotropic, and if $|\Psi| > 6^\circ$, then the subsurface structure is 3-D or azimuthally anisotropic [Booker, 2014]. Normalized skew angles are larger than this threshold for most stations in the period range 0.1–200 s, indicating the need for 3-D modeling (Figure 5). Furthermore, the survey area is near the Southern Ocean, which can have an effect on MT responses and needs to be included in the modeling.

Regional geoelectric strike was estimated from the 2-D parts of the MT response and induction vectors, constrained by values of Ψ and ϵ . Within a spread of strike estimations across each decade, a median value of 35° east of geographic north (with an ambiguity of 90°) persists. The 90° ambiguity in this direction suggests that the electric strike could be responding either to the coast or to the geological features, which strike approximately perpendicular to the coast. Induction arrows, where measured, show complex responses that may indicate contributions from both the ocean and the local geology (Figure 5). Stations S14, S16–S18, and L01 have phases above 90° in the Z_{yx} mode when rotated to geoelectric strike for periods greater than 100 s.

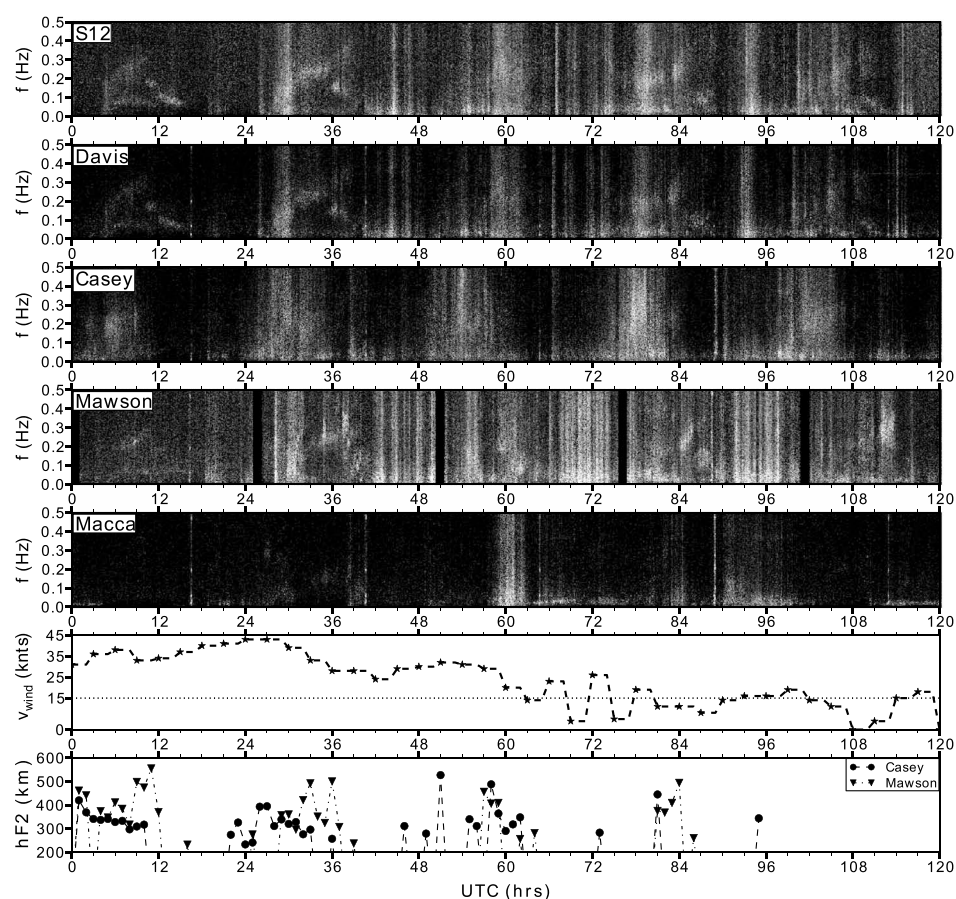


Figure 4. Spectrograms, calculated by equation (A3) with $M=512$, $L=11$, and $\alpha=0.38$, of magnetic field data aligned with geomagnetic north measured simultaneously at various locations in Antarctica for Julian days 012–016. The color map represents normalized power in decibels where white is 1 dB and black is -35 dB. Plotted at the bottom are wind speed in m/s and height of the F_2 layer in kilometers as measured from Casey and Mawson stations (note that data are sparse and measured at sporadic times). A periodic signal starts at around 0600 UT and ends at 1800 UT each day and correlates with increased height of the F_2 layer (hF_2). This supports the postulation by Martyn [1953] and observations made by King *et al.* [1971] that Hall currents are associated with a lift in the ionospheric F_2 layer.

6. Modeling

To model the MT data, both 2-D and 3-D inversion algorithms were used. For 2-D inversions, the Occam algorithm developed by deGroot-Hedlin and Constable [1990] was employed, and only the TM mode and induction vectors for the stations in Figure 5 were used. Using only the TM mode reduces 3-D effects from 2-D inversions [Wannamaker *et al.*, 1984]. Modeling the data in both 2-D and 3-D permits testing the importance of using 3-D inversions to model MT data along a 2-D profile, similar to Siripunvaraporn *et al.* [2005a].

The 2-D model mesh had horizontal cells of 500 m within the station area and cell size increased exponentially outward to 200 km in each direction to prevent any edge effects. Vertical cells increased exponentially from 100 m thick to 300 km thick with depth. The total grid size was 148×80 cells. Data were rotated to a strike direction of 35° east of geographic north, where the profile line was oriented perpendicular to strike. Since the profile is approximately parallel to the coast, the ocean could not be included in the model. Twenty-four periods from 0.08 to 218 s were included in the inversion. All data points with phases above 90° were excluded from the inversion, which included stations south of S14 for periods longer than 100 s. To give more weight to the impedance phases and to accommodate any remaining static shifts that had not been corrected using the median method, a phase error floor of 0.7125° was used and an apparent resistivity error floor of 10%. From different starting models, the lowest normalized root-mean-square (nRMS) error was found from a 500 Ωm half-space. From this model the lowest nRMS was 3.2 after 12 iterations. The model was restarted from a 500 Ωm half-space with a target nRMS of 3.3 to produce a smooth model.

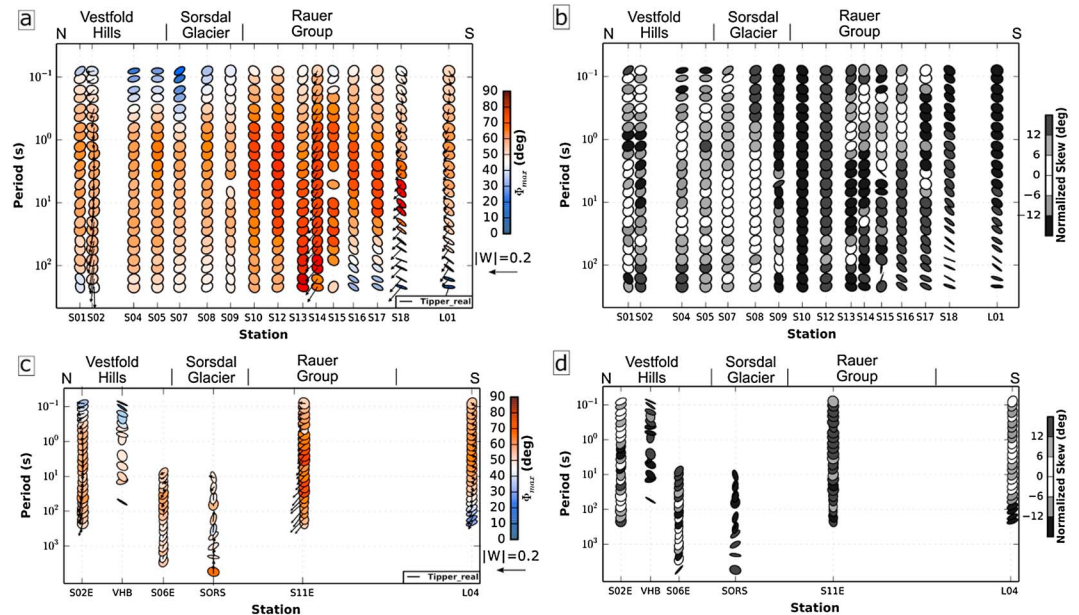


Figure 5. (a and b) Phase tensor pseudosections of stations used in 2-D modeling and (c and d) additional stations used in 3-D modeling, with geographic locations of important features. Figures 5a and 5c are colored by the maximum phase principle component of the phase tensors, which illustrates relative changes in resistivity structure as a function of period. The real part of the induction vector is represented as a black arrow where measured. White colors represent no change in resistivity with increasing period, while cool colors represent increasing resistivity and warm colors represent decreasing resistivity. There is a sharp boundary at the southern edge of the Sørsdal Glacier. Figures 5b and 5d are colored by the normalized skew angle of Booker [2014] representing dimensionality as described in the text.

For 3-D modeling, both the minimum structure algorithm of Siripunvaraporn *et al.* [2005b] (WS) and the nonlinear conjugate method of Egbert and Kelbert [2012] (ModEM) were used. For both methods, the horizontal cell size was 1.5 km within the survey area while outside the survey area increasing padding of cells produced a model width of 400 km. Vertical layer thicknesses increased exponentially from 100 m to 300 km. The WS mesh was $59 \times 27 \times 35$ cells and incorporated 18 stations. All components of \mathbf{Z} were inverted for eight periods between 0.08 and 150 s. The ModEM mesh was $85 \times 55 \times 35$ cells and contained all components of \mathbf{Z} and induction vectors (where measured) for 22 stations, which were inverted for 11 periods in the range 0.08–3000 s. More periods and induction data can be incorporated in ModEM than WS; hence, ModEM has more input data. Both model grids were aligned with geographic north since the large diagonal components mean that any grid rotations have only minor effects. Both models included the ocean ($0.3 \Omega\text{m}$). Modeling was carried out in a multistep process. To begin, larger error floors (20% and 50% for off-diagonal and diagonal components of \mathbf{Z} for WS and $0.12 \sqrt{Z_{xy}Z_{yx}}$ for ModEM) were placed on the data, and the smoothing parameters were set to produce a smooth model ([5, 0.3, 0.3, 0.3] for WS and 0.6 for the covariance of ModEM). The model with the lowest nRMS error was then used as a starting model for data with smaller error bars (5% and 20% for off-diagonal and diagonal components of \mathbf{Z} for WS and $0.03 \sqrt{Z_{xy}Z_{yx}}$ for ModEM) and rougher smoothing constraints ([5, 0.1, 0.1, 0.1] for WS and 0.3 for the covariance of ModEM). Multiple starting models were used including half-spaces of 10, 100, 500, 1000, and 10,000 Ωm .

Both inversions are deterministic and nonunique, so many models can fit the data equally. Therefore, all anomalies in the resistivity models were tested for robustness by (1) removing the anomaly, locking its cells with background values, and rerunning the inversion, (2) changing the resistivity of the anomaly and forward modeling the response to test the sensitivity to the resistivity value, and (3) trimming the anomaly and forward modeling the response. The models produced by the different modeling codes were similar, and the comparison of the preferred 2-D model and preferred 3-D model is in Figure 6. The dominant strike of features in the 3-D model supports the choice of strike in the 2-D model. The model discussed below is the preferred ModEM model, which achieved a nRMS of 2.3 (see supporting information for data and model fits for both the 2-D and 3-D inversions).

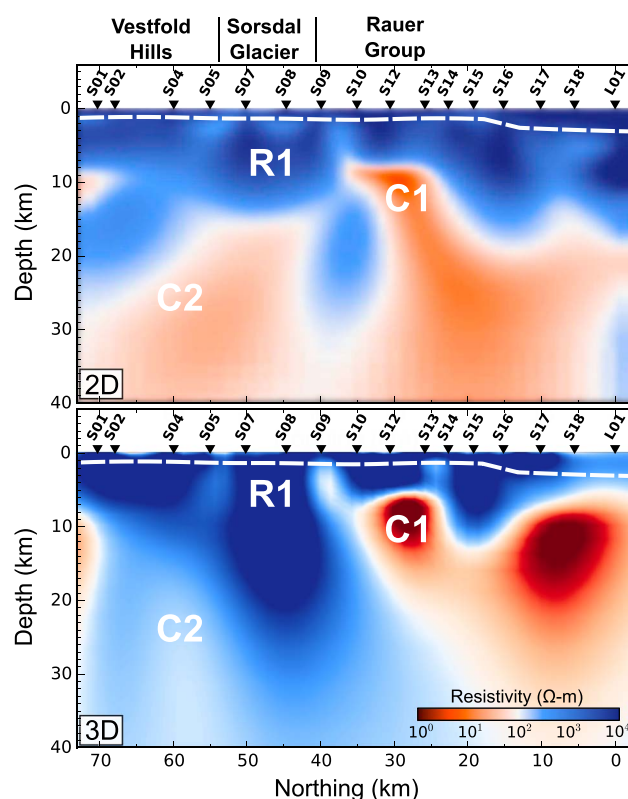


Figure 6. Comparison of the preferred (top) 2-D and (bottom) 3-D models along the S stations. The white dashed line represents the bottom of the ice cap [Fretwell *et al.*, 2013], and C1, C2, and R1 are anomalies discussed in the text.

6.1. Two-Dimensional Versus 3-D Modeling

The preferred 2-D model is similar to the preferred 3-D model, and both models image three main anomalies: C1, C2, and R1 (Figure 6). Conductor C1 ($\sim 10 \Omega\text{m}$) has a maximum conductivity at a depth of 10 km in the 2-D model, before continuing with a southerly dip to at least 30 km depth and also extending to the south with a lower conductivity. In the 3-D model, C1 has a higher conductivity ($< 1 \Omega\text{m}$) and a larger conductance than in the 2-D model and the conductive extension to the south is larger and shallower. These differences are largely due to the masking of phases larger than 90° for periods longer than 1 s at stations south of station S14 in the 2-D inversion. Therefore, the 3-D resistivity model has better resolution of C1 and the southern end of the model. Resistor R1 is similar in both models, but in the 3-D model, it is more resistive, has more distinct boundaries, and extends to greater depth. In contrast, feature C2 differs significantly between the two models. It is much more pronounced in the 2-D model where it is imaged as a zone of lower resistivity ($\sim 50 \Omega\text{m}$) and higher conductance than in the 3-D model. Data fits for the TM mode are similar for the 2-D and 3-D models. However, C2 is better constrained in the 3-D model since this model incorporated all components of the impedance tensor and the 3-D model incorporates the oceanic effect, where the 2-D model does not. The larger conductance could be an influence of the ocean, which the TM mode would be sensitive to. This exemplifies the need to use 3-D modeling in areas near oceans and in areas where the MT response displays 3-D geometry.

7. Discussion

7.1. Factors Affecting MT Data in Antarctica

Analysis of MT transfer function estimates from different times showed that the best time to measure transfer functions was between 1000 and 1400 UT. Two reasons can be hypothesized. First, poor coherences between electric and magnetic fields in the period band 0.2–100 s arise when ground wind speeds exceed $\sim 8 \text{ m/s}$. In the austral summer, katabatic winds near Davis Station begin to blow from the geographic South Pole toward the shore around 2000–0400 UT. These winds do not cause the cables to move, as the cables melt into the snow and ice soon after deployment, but instead, the winds pick up innately charged snow particles

that accumulate in near-surface clouds that can exceed 2 m in height and produce spurious electric fields, as described by Wannamaker *et al.* [2004]. The frequency and strength of these electric fields depend on the size of the particle clouds, their net charge, and wind speed. The vertical component of the magnetic field is more strongly affected during windy times than the horizontal components, confirming that the blowing snow cloud has a net charge as found by Burrows and Hobbs [1970]. Spectrograms of electric and vertical magnetic field data reveal white noise for wind speeds above ~ 8 m/s in the period range of about 0.2–100 s (Figure 4). This is a wider band than found by Wannamaker *et al.* [2004], who were dealing with general storminess rather than katabatic winds.

The second reason for estimating the MT transfer function between 1000 and 1400 UT is because a periodic magnetic signal in the period range of 2–40 s occurs daily during this time window. This event coincides with the UT controlled diurnal variations of the ionosphere's F_2 layer in the austral summer postulated by King *et al.* [1971]. These authors suggest that ionospheric variations are caused by vertical drifts of ions in the F_2 layer created by horizontal neutral thermospheric winds. The vertical movements of ions are influenced by horizontal magnetic fields from the magnetosphere generating a slowly varying (2–40 s) Hall current that flows antiparallel to natural horizontal magnetic fields [Martyn, 1953]. The Hall currents are assumed to be planar because the height of the F_2 layer is above 300 km [King *et al.*, 1971]. Fortunately, these currents enhance the magnetic fields impinging on the Earth, thus increasing coherence of the MT response, especially in the natural deadband.

Covariant PCA results suggest that nonplanar source field effects are minimal, which is in agreement with Beblo and Liebig [1990], Wannamaker *et al.* [1996], and Wannamaker *et al.* [2004]. Results show that two principal components occur within the period range of 2–3000 s, while a third is rarely observed. Usually, when a third is present, there appears to be no correlation with wind or anomalous signal in the magnetic spectrogram. Estimating covariant apparent resistivity locates more time windows when source field effects may be present, especially in the presence of wind noise above 8 m/s. These observations suggest that nonplanar source fields do not significantly impact MT data collected near Davis Station in East Antarctica.

7.2. Model Interpretation

This survey was not designed to investigate the ice cap, but the uppermost ~ 2 km of the resistivity model images the ice cap (Figure 6) and highlights the potential utility of MT in glacial environments. Ice thickness is ~ 2 km over most of the study area [Fretwell *et al.*, 2013] which correlates well with the 2 km thick resistor ($>10,000 \Omega\text{m}$) in the uppermost part of the resistivity model. This resistivity is slightly lower than those typical of pure glacial ice ($>100,000 \Omega\text{m}$), which could be due to poor resolution of the absolute resistivity of resistors in MT data and the possible presence of dust or salt contaminants in the ice [e.g., Taylor *et al.*, 1993]. The Sørdsdal Glacier is imaged as a resistor that extends from the coast to at least 40 km inland along a topographic low imaged by Fretwell *et al.* [2013] (Figure 7b). The resistive valley dips toward the ocean and is up to 2–3 km deep (Figures 7d and 7f). A thin (<100 m) conductor directly underlies the glacial ice cap, which can be interpreted to be caused by till layers saturated with meltwater [Weertman, 1972]. Similarly, several conductive anomalies lie beneath the resistive ice cap, including two under the Sørdsdal Glacier and another farther east, which are most likely thick till layers or even subglacial lakes (SGL) with enhanced ion contents (Figure 7c).

The upper crust in the MT model is moderately resistive ($<2000 \Omega\text{m}$) and typical of crystalline rocks at crustal temperatures [Selway, 2014]. At greater depths (>8 km), a stark contrast is apparent between the northern part of the model (inland of the outcropping Vestfold Hills) which largely retains high resistivities $>1000 \Omega\text{m}$ to upper mantle depths, and the southern part of the model (inland of the outcropping Rauer Group) which demonstrates much lower resistivities <100 to $<10 \Omega\text{m}$ (Figure 7). Low resistivities are also modeled beneath the outcropping Vestfold Hills and Rauer Group, although these are less well constrained by sparse MT station coverage. Comparison with magnetic data from the Antarctic Digital Magnetic Anomaly Project (ADMAP) [Golynsky *et al.*, 2006a] shows a remarkable correlation between regions of high magnetic susceptibility and high conductivity (Figure 7). High-amplitude (~ 600 nT) magnetic anomalies in the Rauer Group and most of the Vestfold Hills have been interpreted to be caused by Archean gneisses [Golynsky *et al.*, 2002; McLean *et al.*, 2009], similar to the Crooked Lake Gneiss in the Vestfold Hills that have a measured magnetic susceptibility of $0.4\text{--}227 \times 10^{-3}$ nT [Golynsky *et al.*, 2006b]. Unfortunately, no magnetic susceptibilities have been recorded for Rauer Group Archean gneisses. It is likely that the abundant mafic dikes in the region are also a significant contributor to the regional anomalies since recorded magnetite contents in the dikes are as

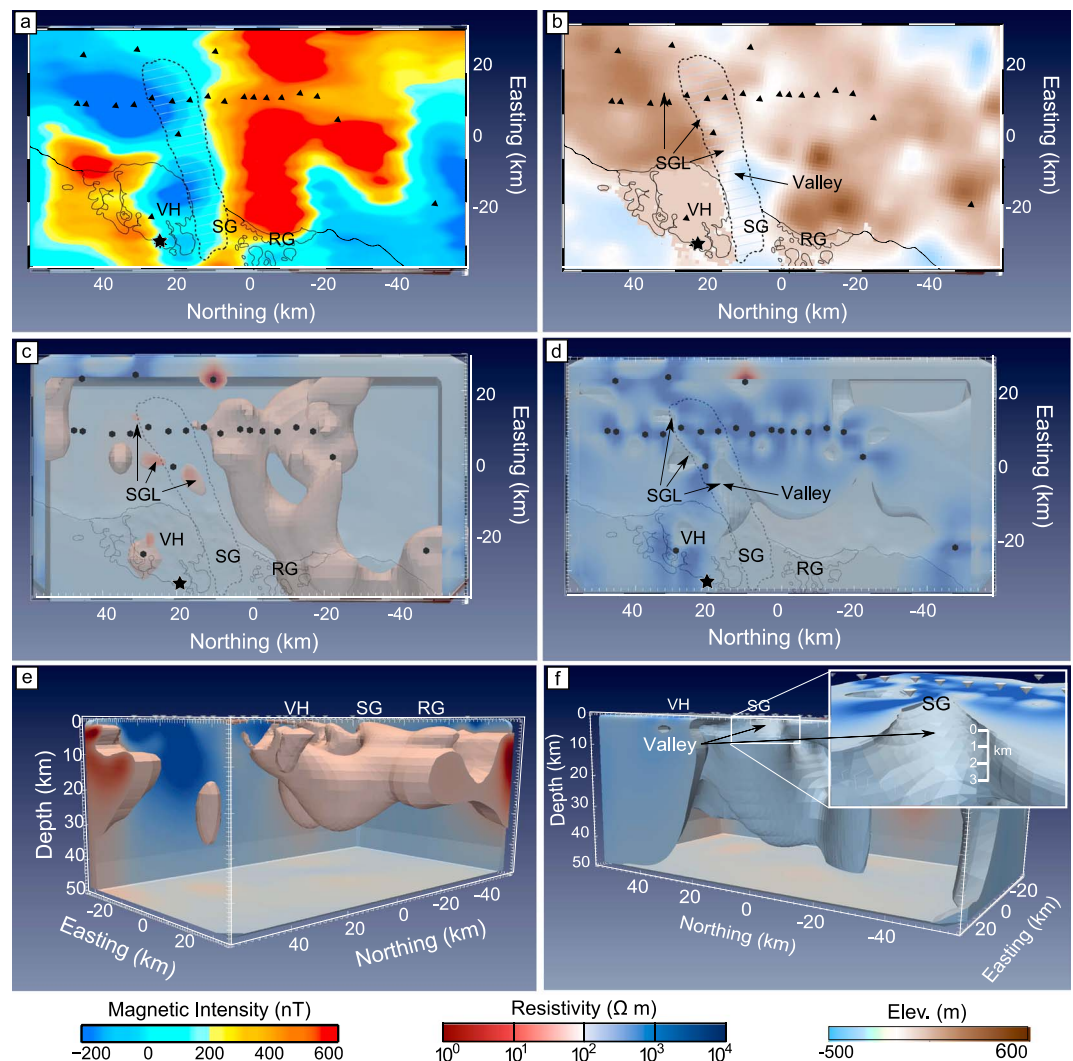


Figure 7. Views of conductive and resistive anomalies within the 3-D resistivity model along with magnetic and basement elevation data. (a) Total magnetic intensity from ADMAP [Golynsky *et al.*, 2006a] shows that the northern Vestfold Hills and the Rauer Group and its inland extent have high magnetic intensities while the Sørsdal Glacier, the southern Vestfold Hills, and the inland extent of the Vestfold Hills have low magnetic intensities. (b) Elevation (meters above sea level) of basement rocks from BEDMAP [Fretwell *et al.*, 2013]. (c) Top view of conductive parts of the preferred 3-D MT model ($<100 \Omega\text{m}$). (d) Top view of resistive parts of the preferred 3-D MT model ($>500 \Omega\text{m}$). (e) View of modeled bodies with resistivities $<100 \Omega\text{m}$ from the southeast. (f) View of modeled bodies with resistivities $>500 \Omega\text{m}$ from the northeast. Inset shows a closeup of the valley containing the Sørsdal Glacier. The star is Davis Station, and black cones are station locations. Seismic receiver function data indicate a crustal thickness of 36 km at Davis station [Reading, 2006]. Labels are VH: Vestfold Hills, SG: Sørsdal Glacier, RG: Rauer Group, and SGL: Interpreted subglacial lake.

large as 3.5% [Delor and Rock, 1991], which would produce magnetic susceptibilities significantly higher than even the highest of those measured in the Crooked Lake Gneiss.

Dikes in both the Vestfold Hills and Rauer Group contain abundant clinopyroxene, orthopyroxene, plagioclase, and biotite [Lanyon *et al.*, 1993]. Minerals in the dikes are iron rich, and samples described by Lanyon *et al.* [1993] have a mean Mg# ($\text{Mg}/(\text{Mg} + \text{Fe})$) of 42. Schmidbauer *et al.* [1996, 2000] showed that the electrical conductivity of amphibole is strongly dependent on iron content. The work of these authors and further research by Wang *et al.* [2012] showed that conductivity can be further increased by dehydration of amphibole as ferrous iron is oxidized to ferric iron. However, a compilation of these results shows that iron-rich amphibole cannot explain the high conductivities observed at midcrustal depths, although it is likely to contribute to enhanced overall crustal conductivity in heavily diked regions (Figure 8). The abundance of hydrous minerals suggests that clinopyroxene is likely to have a high water content, but this is also unable to account for

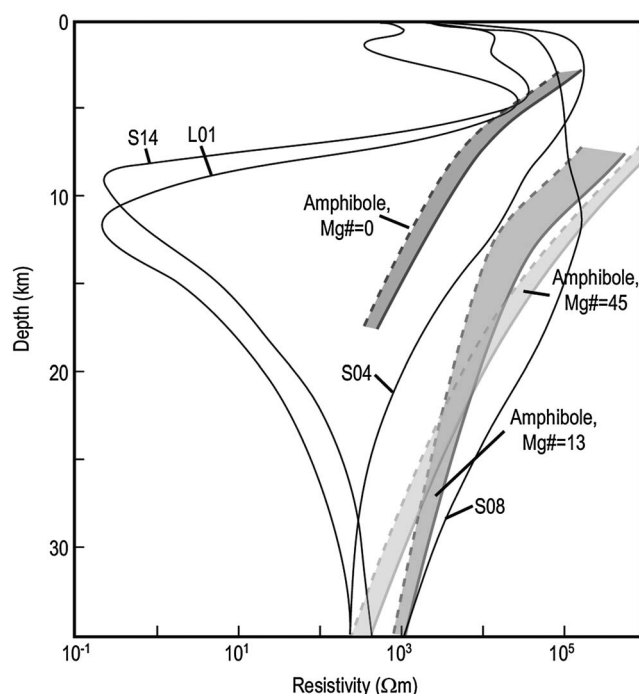


Figure 8. Resistivity/depth sections for stations S14 and L01 from the southern end of the profile, stations S08 and S04 from the northern end of the profile, and laboratory hydrous amphibole resistivity data, assuming a standard stable continental crustal geotherm. $Mg\# = 100 \cdot (Mg / (Mg + Fe))$, $Mg\# = 0$ data are from Schmidbauer *et al.* [1996], $Mg\# = 13$ data are from Schmidbauer *et al.* [2000], and $Mg\# = 45$ data are from Wang *et al.* [2012]. The dashed, low-resistivity limits of the amphibole resistivity data are from dehydrated samples. The resistivity of hydrous clinopyroxene is too high to be shown in this figure.

the very high observed conductivities [Yang *et al.*, 2011]. Guo *et al.* [2015] have recently shown that very small amounts of water or brine in a quartz-albite mix can produce very high conductivities, but free fluid would not be expected to be present in the stable middle to lower crust of the Vestfold Hills and Rauer Group.

Sulfide minerals, including sulfide grain-boundary films, can produce very high conductivities [Watson *et al.*, 2010]. Dikes from the Vestfold Hills contain massive sulfide minerals and also contain bravoite, sulpharsenides, and tellurides as grain boundary films with thicknesses as little as 10–20 μm [Seitz and Keays, 1997]. Dikes from the Rauer Group also contain sulfide minerals including pyrite and chalcopyrite [Sims *et al.*, 1994]. The presence of carbonates in dikes in the Vestfold Hills [Delor and Rock, 1991] and calcite veins and alteration zones in dikes in the Rauer Group [Sims *et al.*, 1994] suggests that graphite may also contribute to the high observed conductivities, either in connected flakes or, more likely, in grain-boundary graphite films [Frost *et al.*, 1989]. It is also possible that these conductive minerals exist in the country rocks [e.g., Boerner *et al.*, 1996], although this is more speculative since they have not been observed in these rocks. Therefore, conductive anomaly C1 is interpreted to be due to sulfide minerals, sulfide grain-boundary films, and/or graphite grain-boundary films within dikes that contain iron-rich and hydrogen-rich amphibole and clinopyroxene. The conductive anomalies do not extend to the upper crust due to a combination of low temperatures and disconnection of the grain-boundary films at low pressures. The dikes and country rocks also contain significant volumes of magnetite and are therefore associated with positive magnetic anomalies.

Resistive anomaly R1, which lies directly beneath the Sørsdal Glacier, is associated with a clear decrease in magnetic intensity and is also electrically resistive to upper mantle depths. Given that a suture between the Rauer Group and Vestfold Hills is likely to lie beneath the Sørsdal Glacier, it is possible that the low magnetic intensity and high resistivity are associated with the suture. Metamorphism associated with suturing, especially under oxidizing conditions, could produce such a result. During high-temperature metamorphism, ferromagnetic magnetite (Fe^{2+}) will be oxidized to paramagnetic hematite (Fe^{3+}) with an associated decrease in magnetic susceptibility [e.g., Pullaiah *et al.*, 1975]. In addition, metamorphism in oxidizing conditions will destroy graphite since it is only stable in reducing conditions and will be converted to CO_2 in oxidizing conditions [Holloway, 1984]. Furthermore, sulfide minerals can also be destroyed in oxidizing metamorphic

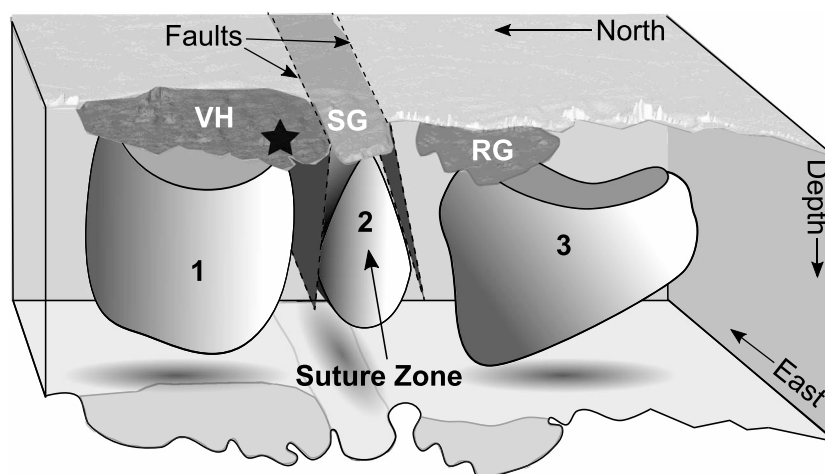


Figure 9. Geological interpretation of the three geophysically distinct zones in the subsurface near Davis Station (black star), East Antarctica. Zone 1, which lies beneath the northern outcropping Vestfold Hills (VH), and zone 3, which lies beneath the outcropping Rauer Group (RG) and its inland extent, have high electrical conductivities and magnetic intensities due to the presence of magnetite, sulfides, and graphite in dikes and possibly country rocks. In the southern VH and beneath the Sørsdal Glacier (SG; zone 2), these minerals have been oxidized by metamorphic processes most likely related to suturing, resulting in a decrease in electrical conductivity and magnetic intensity. The region inland of the VH also displays low electrical conductivity and magnetic intensity, which may indicate that this region was also metamorphosed during suturing or that it was never intruded by dikes.

conditions, particularly in the presence of water [Rimstidt and Vaughan, 2003], in reactions such as FeS_2 (pyrite) + $3.5 \text{ O}_2 + \text{H}_2\text{O} = \text{Fe}^{2+} + 2\text{H}^+ + 2\text{SO}_4^{2-}$. The low magnetic intensity and high resistivity beneath the Sørsdal Glacier are surmised to be caused by the destruction of magnetic and conductive minerals during suture-related metamorphism.

Geological interpretation of the electrical resistivity model is summarized in Figure 9. From the Archean to at least the Mesoproterozoic, the Vestfold Hills and Rauer Group were separate from each other and attached to different paleocontinents. During this time, protoliths to each region formed and tectonized, with both regions intruded by voluminous mafic dikes. These dikes (and potentially surrounding country rocks) contained abundant magnetite, sulfides, and probably graphite, giving both regions high magnetic susceptibility and high electrical conductivity. When suturing occurred between the Vestfold Hills and Rauer Group, the associated high-temperature metamorphism oxidized the magnetite, sulfides, and graphite. This produced a region of low magnetic susceptibility and low electrical conductivity in the metamorphosed suture zone, which is imaged beneath the Sørsdal Glacier.

The two most likely possibilities for the timing of suturing are (1) during the Mesoproterozoic to Neoproterozoic metamorphism observed in the southern Vestfold Hills [Clark *et al.*, 2012] and (2) during Gondwana amalgamation in the Pan-African. While MT data cannot constrain this timing, petrologic, geochemical, electrical resistivity, and magnetic susceptibility of surface exposures would help correlate observations in this study and guide chronological order of tectonic events. Absence of outcropping Pan-African rocks in the Vestfold Hills makes the second hypothesis a challenge to test. The cause of the high resistivities inland of the Vestfold Hills is uncertain due to the absence of outcrop in this region. However, based on the above interpretation, high resistivities are caused either by an absence of dikes (i.e., conductive minerals were never introduced into the crust) or by subsequent suture-related metamorphism. More MT data should be collected to constrain the areal extent of the outcropping rocks under the ice.

8. Conclusion

Magnetotelluric data have been successfully collected in Prydz Bay, East Antarctica. Preamplifiers were used to overcome the high contact resistance of ice. Time-frequency analysis of the MT time series data reveals the best time to measure is between 1000 and 1400 UT when katabatic winds are minimal and activity in the magnetosphere is high. A preferred 3-D resistivity model developed from the MT data reveals zones of extremely high crustal conductivity that correspond with regions of high magnetic intensity, interpreted to be

caused by magnetite, sulfides, and possibly graphite in voluminous dikes that outcrop in the Vestfold Hills and Rauer Group. A crustal resistor that is associated with a region of low magnetic intensity underlies the Sørdsdal Glacier. This glacier separates the Vestfold Hills and Rauer Group and extends at least 40 km inland along a topographic low. We interpret that the low conductivity and magnetic intensity are due to the breakdown of magnetite, sulfides, and graphite during metamorphism associated with suturing of the Vestfold Hills and Rauer Group. Ice thickness within the survey area was modeled to be ~2 km and at least four regions of sub-ice high conductivity were imaged, including one beneath the Sørdsdal Glacier, which are likely to be subglacial lakes or saturated till layers. This experiment demonstrates that challenges associated with collecting MT data in Antarctica can be overcome and that MT has great potential for imaging Antarctic sub-ice geology as well as ice sheet and glacial features.

Appendix A: Time-Frequency Distributions

Time-frequency distributions represent a signal covariant in time and frequency by transforming short time windows into harmonic functions, visually represented as a spectrogram [Boashash, 2003]. The short time Fourier transform (STFT) is the simplest method, but unfortunately, resolution is restricted by length of the time window as dictated by the Heisenberg uncertainty principle. Quadratic functions based on the Wigner-Ville distribution (WVD) have been developed which perfectly localize monochromatic signals. However, due to its quadratic nature, multicomponent signals will have cross terms. Reduction of these cross terms have been the subject of intensive study the past few decades [Cohen, 1989; Boashash, 2003; Sejdic et al., 2009]. An elegant and efficient method to exploit the resolution of the WVD while minimizing cross terms is the S-method [Stankovic, 1994]. One advantage is that the analytic signal does not need to be calculated like other quadratic representations. The S-method starts with the STFT and adds correction terms from nearby time-frequency points moving toward the WVD, where the optimum radius is large enough to not include cross terms.

In noisy environments, the spectrogram can be distorted and difficult to interpret. Therefore, Djurovic et al. [2001] introduced a robust STFT employing a simple vector median filter based on Huber's robust statistics to remove impulse noise. This was extended by Djurovic et al. [2003] to Huber's L-estimate, which filters signal contaminated by a mixture of Gaussian and impulse noise, similar to robust MT transfer function estimation methods developed by Chave and Thomson [2004] and Egbert [1997]. Equation (A1) formulates the STFT L-estimate of a discrete time series $z[n]$, where n and k are discrete time and frequency, M is the length of window $h[n]$, x_j and y_j are in nondescending order (similar to estimating the median), and $\alpha \in [0, .5]$ is a weighting parameter, equation (A2). A robust S-method can be computed from the STFT L-estimate, equation (A3).

$$\text{STFT}_L[n, k] = \sum_{j=0}^{M-1} a_j (x_j[n, k] + i y_j[n, k]), \quad (A1)$$

$$x_j \in [\text{Re}\{h[n]z[n+m]e^{i2\pi km/M}\}; m \in [0, M-1]]$$

$$y_j \in [\text{Im}\{h[n]z[n+m]e^{i2\pi km/M}\}; m \in [0, M-1]]$$

$$a_j = \begin{cases} \frac{1}{M(1-2\alpha)+4\alpha} & j \in [(M-2)\alpha, \alpha(2-M)+M-1] \\ 0 & \text{elsewhere} \end{cases} \quad (A2)$$

$$SM_x[n, k] = |\text{STFT}_L[n, k]|^2 + 2 \sum_{l=0}^L \text{STFT}_L[n, k+l] \text{STFT}_L^*[n, k-l] \quad (A3)$$

References

- Banks, R. J. (1998), The effects of non-stationary noise on electromagnetic response estimates, *Geophys. J. Int.*, **135**, 553–563, doi:10.1046/j.1365-246x.1998.00661.x.
- Beblo, M., and V. Liebig (1990), Magnetotelluric measurements in Antarctica, *Phys. Earth Planet. Inter.*, **60**, 89–99, doi:10.1016/0031-9201(90)90251-r.
- Bibby, H. M., T. G. Caldwell, and C. Brown (2005), Determinable and non-determinable parameters of galvanic distortion in magnetotellurics, *Geophys. J. Int.*, **163**, 915–930, doi:10.1111/j.1365-246X.2005.02779.x.

Acknowledgments

Field work was funded by the Australian Antarctic Division Grant 2771 (Chief Investigator A. Collins, University of Adelaide). AuScope provided instruments and some additional funding. Extremely helpful technical support was provided by G. Boren and G. Heinson, University of Adelaide. During this work, J.R.P. was supported by International Postgraduate Research Scholarship at the University of Adelaide. K.S. was supported by Australian Research Council grants LP0774891 and DP0988263 and Research Council of Norway Centre of Excellence project 223272. In addition to logistical support, the Australian Antarctic Division provided archived magnetic time series and hF_2 data. The authors are grateful to Pete Carrigan, Jason Watson, and Campbell Harvey for their invaluable assistance with field work and to Phil Wannamaker, John Stodt, and Louise Pellerin for advice on collecting MT data in Antarctica. The manuscript was greatly improved by comments from two anonymous referees. This is TraX publication number 350. The data are available upon request. Any use of trade, firm, or product names is for descriptive purposes only and does not imply endorsement by the U.S. Government.

- Black, L. P., S. L. Harley, S. S. Sun, and M. T. McCulloch (1987), The Rayner complex of East Antarctica: Complex isotopic systematics within a Proterozoic mobile belt, *J. Metamorph. Geol.*, **5**, 1–26, doi:10.1111/j.1525-1314.1987.tb00366.x.
- Boashash, B. (Ed.) (2003), *Time Frequency Signal Analysis and Processing: A Comprehensive Reference*, Elsevier, Amsterdam.
- Boerner, D. E., R. D. Kurtz, and J. A. Craven (1996), Electrical conductivity and Paleoproterozoic foredeeps, *J. Geophys. Res.*, **101**, 13,775–13,791, doi:10.1029/96JB00171.
- Boger, S. D., C. J. L. Wilson, and C. M. Fanning (2001), Early Paleozoic tectonism within the East Antarctic craton: The final suture between east and west Gondwana, *Geology*, **22**, 307–310, doi:10.1130/0091-7613(2001)029<0463:eptwte>2.0.co;2.
- Booker, J. R. (2014), The magnetotelluric phase tensor: A critical review, *Surv. Geophys.*, **35**, 7–40, doi:10.1007/s10712-013-9234-2.
- Burrows, D. A., and P. V. Hobbs (1970), Electrical charges on snow particles, *J. Geophys. Res.*, **75**, 4499–4505, doi:10.1029/JC075i024p04499.
- Caldwell, T. G., H. M. Bibby, and C. Brown (2004), The magnetotelluric phase tensor, *Geophys. J. Int.*, **158**, 457–457, doi:10.1111/j.1365-246X.2004.02203.x.
- Chant, I. J., and L. M. Hastie (1992), Time-frequency analysis of magnetotelluric data, *Geophys. J. Int.*, **111**, 399–413, doi:10.1111/j.1365-246X.1992.tb00586.x.
- Chave, A. D., and A. G. Jones (2012), *The Magnetotelluric Method: Theory and Practice*, Cambridge Univ. Press, New York.
- Chave, A. D., and D. J. Thomson (2004), Bounded influence magnetotelluric response function estimation, *Geophys. J. Int.*, **157**, 988–1006, doi:10.1111/j.1365-246X.2004.02203.x.
- Chi, P. J., and C. T. Russell (2008), Use of the Wigner-Ville distribution in interpreting and identifying ULF waves in triaxial magnetic records, *J. Geophys. Res.*, **113**, A01218, doi:10.1029/2007JA012469.
- Clark, C., P. D. Kinny, and S. L. Harley (2012), Sedimentary provenance and age of metamorphism of the Vestfold Hills, East Antarctica: Evidence for a piece of Chinese Antarctica?, *Precambrian Res.*, **196**, 23–45, doi:10.1016/j.precamres.2011.11.001.
- Cohen, L. (1989), Time-frequency distributions—A review, *Proc. IEEE*, **77**, 941–981, doi:10.1109/5.30749.
- Collins, A. S., and S. A. Pisarevsky (2005), Amalgamating eastern Gondwana: The evolution of the Circum-Indian Orogens, *Earth Sci. Rev.*, **71**, 229–270, doi:10.1016/j.earscirev.2005.02.004.
- deGroot-Hedlin, C., and S. Constable (1990), Occam's inversion to generate smooth, two-dimensional models from magnetotelluric data, *Geophysics*, **55**, 1613–1624, doi:10.1190/1.1442813.
- Delor, C., and N. Rock (1991), Alkaline-ultramafic lamprophyre dykes from the Vestfold Hills, Princess Elizabeth Land (East Antarctica): Primitive magmas of deep mantle origin, *Antarct. Sci.*, **3**, 419–432, doi:10.1017/S0954102091000512.
- Djurovic, I., V. Katkovnik, and L. Stankovic (2001), Median filter based realizations of the robust time-frequency distributions, *Signal Process.*, **81**, 1771–1776, doi:10.1016/S0165-1684(01)00092-5.
- Djurovic, I., L. Stankovic, and J. F. Bohme (2003), Robust L-estimation based forms of signal transforms and time-frequency representations, *IEEE Trans. Signal Process.*, **51**, 1753–1761, doi:10.1109/TSP.2003.812739.
- Egbert, G. D. (1997), Robust multiple-station magnetotelluric data processing, *Geophys. J. Int.*, **130**, 475–496, doi:10.1111/j.1365-246X.1997.tb05663.x.
- Egbert, G. D. (2002), Processing and interpretation of electromagnetic induction array data, *Surv. Geophys.*, **23**, 207–249, doi:10.1023/A:1015012821040.
- Egbert, G. D., and A. Kelbert (2012), Computational recipes for electromagnetic inverse problems, *Geophys. J. Int.*, **189**, 251–267, doi:10.1111/j.1365-246X.2011.05347.x.
- Flowerdew, M., S. Tyrrell, S. Boger, I. Fitzsimons, S. Harley, E. Mikhalsky, and A. Vaughan (2013), Pb isotopi domains from the Indian Ocean sector of Antarctica: Implications for past Antarctica-India connections, *Geol. Soc. London Spec. Publ.*, **383**, 59–72, doi:10.1144/sp383.3.
- Fretwell, P., et al. (2013), Bedmap2: Improved ice bed, surface and thickness data for Antarctica, *Cryosphere*, **7**, 375–393, doi:10.5194/tcd-6-4305-2012.
- Frost, B. R., W. S. Fyfe, K. Tazaki, and T. Chan (1989), Grain-boundary graphite in rocks and implications for high electrical conductivity in the lower crust, *Nature*, **340**, 134–136, doi:10.1038/340134a0.
- Golynsky, A., S. Alyavdin, V. Masolov, A. Tschernin, and V. Volnukhin (2002), The composite magnetic anomaly map of East Antarctica, *Tectonophysics*, **347**, 109–120, doi:10.1016/S0040-1951(01)00240-2.
- Golynsky, A., M. Chiappini, D. Damaske, F. Ferraccioli, C. A. Finn, T. Ishihara, H. R. Kim, L. Kovacs, V. N. Masolov, and P. Morris (2006a), ADMAP—A digital magnetic anomaly map of the Antarctic, in *Antarctica*, edited by D. K. Fütterer et al., pp. 109–116, Springer, Berlin, doi:10.1007/3-540-32934-x_12.
- Golynsky, A. V., V. N. Masolov, V. S. Volnukhin, and D. A. Goylnsky (2006b), Crustal provinces of the Prince Charles Mountains region and surrounding areas in the light of aeromagnetic data, in *Antarctica*, edited by D. K. Fütterer et al., pp. 83–94, Springer, Berlin, doi:10.1007/3-540-32934-x_0.
- Guo, X., T. Yoshino, and A. Shimojuku (2015), Electrical conductivity of albite-(quartz)-water and albite-water-NaCl systems and its implications to the high conductivity in the continental crust, *Earth Planet. Sci. Lett.*, **412**, 1–9, doi:10.1016/j.epsl.2014.12.021.
- Harley, S. (2003), Archean-Cambrian crustal development of East Antarctica: Metamorphic characteristics and tectonic implications, *Geol. Soc. London Spec. Publ.*, **206**, 203–230, doi:10.1144/gsl.sp.2003.206.01.11.
- Harley, S., I. Snape, and L. Black (1998), The evolution of a layered metaigneous complex in the Rauer Group, East Antarctica: Evidence for a distinct Archean terrane, *Precambrian Res.*, **89**, 175–205, doi:10.1016/S0301-9268(98)00031-x.
- Harley, S. L., and I. C. W. Fitzsimons (1995), High-grade metamorphism and deformation in the Prydz Bay region, East Antarctica: Terranes, events and regional correlations, *Mem. Geol. Soc. India*, **34**, 73–100.
- Hessler, V. P., and J. Jacobs (1966), A telluric experiment on the Antarctic ice cap, *Nature*, **210**, 190–191, doi:10.1038/210190a0.
- Hoek, J. D., and H. M. Seitz (1995), Continental mafic dyke swarms as tectonic indicators: An example from the Vestfold Hills, East Antarctica, *Precambrian Res.*, **75**, 121–139, doi:10.1016/0301-9268(95)80002-Y.
- Holloway, J. R. (1984), Graphite-CH₄-H₂O-CO₂ equilibria at low-grade metamorphic conditions, *Geology*, **12**, 455–458, doi:10.1130/0091-7613(1984)12<455:gealmc>2.0.co;2.
- Jones, A. G., and J. Spratt (2002), A simple method for deriving the uniform field MT responses in auroral zones, *Earth Planets Space*, **54**, 443–450, doi:10.1186/bf03353035.
- Kaufman, A. A., and G. V. Keller (1981), *The Magnetotelluric Sounding Method*, Elsevier, Amsterdam.
- Kelsey, D. E., R. W. White, C. M. Powell, C. J. L. Wilson, and C. D. Quinn (2003), New constraints on metamorphism in the Rauer Group, Prydz Bay, East Antarctica, *J. Metamorph. Geol.*, **21**, 739–759, doi:10.1046/j.1525-1314.2003.00476.x.
- Kelsey, D. E., B. P. Wade, A. S. Collins, M. Hand, C. R. Sealing, and A. Netting (2008), Discovery of a Neoproterozoic basin in the Prydz belt in East Antarctica and its implications for Gondwana assembly and ultrahigh temperature metamorphism, *Precambrian Res.*, **161**, 355–388, doi:10.1016/j.precamres.2007.09.003.

- King, J. W., D. Eccles, and H. Kohl (1971), The behavior of the Antarctic ionosphere, *J. Atmos. Terr. Phys.*, **33**, 1067–1077, doi:10.1016/0021-9169(71)90127-9.
- Kinny, P. D., L. P. Black, and J. W. Sheraton (1997), Zircon U-Pb ages and geochemistry of igneous and metamorphic rocks in northern Prince Charles Mountains, Antarctica, *AGSO J. Aust. Geol. Geophys.*, **16**, 637–654.
- Lanyon, R., L. P. Black, and H. M. Seitz (1993), U-Pb zircon dating of mafic dykes and its application to the Proterozoic geological history of the Vestfold Hills, East Antarctica, *Contrib. Mineral. Petrol.*, **115**, 184–203, doi:10.1007/bf00321219.
- Larsen, J. C., R. L. Mackie, A. Manzella, A. Fiordelisi, and S. Rieven (1996), Robust smooth magnetotelluric transfer functions, *Geophys. J. Int.*, **124**, 801–819, doi:10.1111/j.1365-246x.1996.tb05639.x.
- Martí, A. (2014), The role of electrical Anisotropy in magnetotelluric responses: From modelling and dimensionality analysis to inversion and Interpretation, *Surv. Geophys.*, **35**, 179–218, doi:10.1007/s10712-013-9233-3.
- Martyn, D. F. (1953), Electric currents in the ionosphere: III. Ionization drift due to winds and electric fields, *Philos. Trans. R. Soc. A*, **246**, 295–305, doi:10.1098/rsta.1953.0018.
- McLean, M., C. Wilson, S. Boger, P. Betts, T. Rawling, and D. Damaske (2009), Basement interpretations from airborne magnetic and gravity data over the Lambert Rift region of East Antarctica, *J. Geophys. Res.*, **114**, B06101, doi:10.1029/2008JB005650.
- Meert, J. G. (2003), A synopsis of events related to the assembly of eastern Gondwana, *Tectonophysics*, **362**, 1–40, doi:10.1016/s0040-1951(02)00629-7.
- Moores, E. M. (1991), Southwest U.S.–East Antarctic (SWEAT) connection: A hypothesis, *Geology*, **19**, 425–428, doi:10.1130/0091-7613(1991)019<0425:SUSEAS>2.3.CO;2.
- Murthy, D. N., K. Veeraswamy, T. Harinarayana, U. K. Singh, and M. Santosh (2013), Electrical structure beneath Schirmacher Oasis, East Antarctica: A magnetotelluric study, *Polar Res.*, **32**, 17309, doi:10.3402/polar.v32i0.17309.
- Parkinson, W. D. (1983), *Introduction to Geomagnetism*, Scottish Acad. Press, Edinburgh.
- Pirjola, R. (1992), On magnetotelluric source effects caused by an auroral electrojet system, *Radio Sci.*, **4**, 463–468, doi:10.1029/92RS00852.
- Pulliaah, G., E. Irving, K. Buchan, and D. Dunlop (1975), Magnetization changes caused by burial and uplift, *Earth Planet. Sci. Lett.*, **28**, 133–143, doi:10.1016/0012-821x(75)90221-6.
- Reading, A. M. (2006), The seismic structure of Precambrian and early Palaeozoic terranes in the Lambert Glacier region, East Antarctica, *Earth Planet. Sci. Lett.*, **244**, 44–57, doi:10.1016/j.epsl.2006.01.031.
- Rickers, K., K. Mezger, and M. M. Raith (2001), Evolution of the continental crust in the Proterozoic EasEast Ghats Belt, India and new constraints for Rodinia reconstruction: Implications from Sm-Nd, Rb-Sr and Pb-Pb isotopes, *Precambrian Res.*, **112**, 183–210, doi:10.1016/s0301-9268(01)00146-2.
- Rimstidt, J. D., and D. J. Vaughan (2003), Pyritie oxidation: A state-of-the-art assessment of the reaction mechanism, *Geochim. Cosmochim. Acta*, **67**, 873–880, doi:10.1016/s0016-7037(02)01165-1.
- Schmidbauer, E., T. Kunzmann, T. Fehr, and R. Hochleitner (1996), Electrical conductivity, thermopower and ^{57}Fe Mössbauer spectroscopy of an Fe-rich amphibole, arfvedsonite, *Phys. Chem. Miner.*, **23**, 99–106, doi:10.1007/bf00202305.
- Schmidbauer, E., T. Kunzmann, T. Fehr, and R. Hochleitner (2000), Electrical resistivity of ^{57}Fe Mössbauer spectra of Fe-bearing catic amphiboles, *Phys. Chem. Miner.*, **27**, 347–356, doi:10.1007/s002690050264.
- Seitz, H. M., and R. R. Keays (1997), Platinum group element segregation and mineralization in a noritic ring complex formed from Proterozoic siliceous high magnesium basalt magmas in the Vestfold Hills, Antarctica, *J. Petrol.*, **38**, 703–725, doi:10.1093/ptroj/38.6.703.
- Sejdic, E., I. Djurovic, and J. Jiang (2009), Time-frequency feature representation using energy concentrations: An overview of recent advances, *Digital Signal Process.*, **19**, 153–183, doi:10.1016/j.dsp.2007.12.004.
- Selway, K. (2014), On the causes of electrical conductivity anomalies in tectectonic stable lithosphere, *Surv. Geophys.*, **35**, 219–257, doi:10.1007/s10712-013-9235-1.
- Sims, J. P., P. H. Dirks, C. J. Carson, and C. J. Wilson (1994), The structural evolution of the Rauer Group, East Antarctica: Mafic dykes as passive markers in a composite Proterozoic terrain, *Antarct. Sci.*, **6**, 379–394, doi:10.1017/s0954102094000581.
- Siripunvaraporn, W., G. Egbert, and M. Uyeshima (2005a), Interpretation of two-dimensional magnetotelluric profile data with three-dimensional inversion: Synthetic examples, *Geophys. J. Int.*, **160**, 804–814, doi:10.1111/j.1365-246X.2005.02527.x.
- Siripunvaraporn, W., G. Egbert, Y. Lenbury, and M. Uyeshima (2005b), Three-dimensional magnetotelluric inversion: Data-space method, *Phys. Earth Planet. Inter.*, **150**, 3–14, doi:10.1016/j.pepi.2004.08.023.
- Smirnov, M. Y., and G. D. Egbert (2012), Robust principal component analysis of electromagnetic arrays with missing data, *Geophys. J. Int.*, **190**, 1423–1438, doi:10.1111/j.1365-246X.2012.05569.x.
- Stankovic, L. (1994), A method for time-frequency analysis, *IEEE Trans. Signal Process.*, **42**, 225–229, doi:10.1109/78.258146.
- Taylor, K. C., C. U. Hammer, R. B. Alley, H. B. Clausen, D. Dahl-Jensen, A. J. Gows, N. S. Gundestrup, J. Kipfstuhl, J. C. Moore, and E. D. Waddington (1993), Electrical conductivity measurements from GISP2 and GRIP Greenland ice cores, *Nature*, **366**, 549–552, doi:10.1038/366549a0.
- Wang, D., Y. Guo, Y. Yu, and S. I. Kurato (2012), Electrical conductivity of amphibole-bearing rocks: Influence of dehydration, *Contrib. Mineral. Petrol.*, **164**, 17–25, doi:10.1007/s00410-012-0722-z.
- Wannamaker, P. E., G. W. Hohmann, and S. H. Ward (1984), Magnetotelluric responses of three-dimensional bodies in layered earths, *Geophysics*, **49**, 1517–1533, doi:10.1071/eg984190c.
- Wannamaker, P. E., J. A. Stodt, and S. L. Olsen (1996), Dormant state of rifting below the Byrd Subglacial Basin, West Antarctica, implied by magnetotelluric (MT) profiling, *Geophys. Res. Lett.*, **23**, 2983–2986, doi:10.1029/96GL02887.
- Wannamaker, P. E., J. A. Stodt, L. Pellerin, S. L. Olsen, and D. B. Hall (2004), Structure and thermal regime beneath the South Pole region, East Antarctica, from magnetotelluric measurements, *Geophys. J. Int.*, **157**, 36–54, doi:10.1111/j.1365-246x.2004.02156.x.
- Watson, H. C., J. J. Roberts, and J. A. Tyburczy (2010), Effect of conductive impurities on electrical conductivity in polycrystalline olivine, *Geophys. Res. Lett.*, **37**, L02302, doi:10.1029/2009GL01566.
- Weertman, J. (1972), General theory of water flow at the base of a glacier or ice sheet, *Rev. Geophys.*, **10**, 287–333, doi:10.1029/RG010i001p00287.
- Wilson, C. J., C. Quinn, L. Tong, and D. Phillips (2007), Early Palaeozoic intracratonic shears and post-tectonic cooling in the Rauer Group, Prydz Bay, East Antarctica constrained by $^{40}\text{Ar}/^{39}\text{Ar}$ thermochronology, *Antarct. Sci.*, **19**, 339–353, doi:10.1017/s0954102007000478.
- Yang, X., H. Keppler, C. McCammon, H. Ni, Q. Xia, and Q. Fan (2011), Effect of water on electrical conductivity of the lower crustal clinopyroxene, *J. Geophys. Res.*, **116**, B04208, doi:10.1029/2010JB008010.